Journal of Advanced Ceramics
2024, **13**(11): 1844–1851
https://doi.org/10.26599/JAC.2024.9220981
Research Article

Flexible and wake-up free $Hf_{0.5}Zr_{0.5}O_2$ ferroelectric thin films with ultra-low operation voltage and high polarization

Jun-Hui Wang[1,2,†], Tian-Peng Duan[2,†], Jia-Jia Liao[1,3,✉], Zhi-Peng Wang[1], Xin-Ran Huang[2], Shi-Jie Jia[1], Ke-Yu Bao[1], Yu-Xin Fan[1], Bing-Jian Zeng[2], Li-Mei Jiang[2], Min Liao[1,2], Yi-Chun Zhou[1], Qiong Yang[2,✉], Jie Jiang[2,✉]

[1] *School of Advanced Materials and Nanotechnology, Xidian University, Xi'an 710126, China*
[2] *School of Materials Science and Engineering, Xiangtan University, Xiangtan 411105, China*
[3] *Guangzhou Institute of Technology, Xidian University, Guangzhou 510555, China*

Received: July 9, 2024; Revised: September 10, 2024; Accepted: September 27, 2024

Abstract: Flexible and transparent hafnium oxide-based ferroelectric films are attracting widespread attention because of the increasing demand for wearable electronic devices. However, the ultra-low voltage operation with robust and stable ferroelectricity, which is a prerequisite for portable device applications, has not been realized simultaneously. Here, we report flexible $Hf_{0.5}Zr_{0.5}O_2$ ferroelectric films with a saturation voltage of only 1.3/3 V and remanent polarization ($2P_r$) of 38/60 μC·cm². Negligible wake-up effect and superior stability resistance to compressive/tensile stress and high temperature up to 150 °C are also demonstrated. The polarization switching dynamics under bending are investigated based on the switching current measurement, suggesting that the intrinsic switching speeds keep almost constant at different bending radii. In addition, there is a negative correlation between the activation field and the compressive or tensile stress, which is due to the lowered energy barrier induced by the in-plane strain applied to the [111]-oriented hexagonal cell. Our work sheds light on the application of flexible, stable, and HfO_2-based ferroelectric thin films with ultra-low consumption.

Keywords: flexible ferroelectrics; $Hf_{0.5}Zr_{0.5}O_2$; ultra-low voltage operation; reliability

1 Introduction

With the increasing demand for wearable electronic devices in the age of intelligence, flexible electronics have attracted increased interest because of their portability, flexibility, light weight, and user friendliness [1–6]. Among them, flexible non-volatile memory is one of the most important devices for information module. Compared with commercialized flash memory, the emerging ferroelectric memory has the advantages of faster speed, better endurance, and lower power consumption [7–9], which benefits from the switchable spontaneous polarization driven by the electric field. Therefore, ferroelectric memory is considered a highly promising candidate for flexible electronics applications.

Recently, considerable efforts have been devoted to developing energy-friendly flexible ferroelectric memory. Several kinds of flexible substrates have been adopted, such as polyimide (PI) [10–12], polyethylene naphthalate (PEN) [13], polyethylene terephthalate (PET) [14], and mica [15,16]. In particular, mica substrates have been widely chosen because they have the advantages of atomically smooth surface, chemical stability, and mechanical flexibility. As flexible ferroelectric thin films are functional materials, their fabrication and performance are the key. Traditional ferroelectrics with perovskite structures (such as lead zirconate titanate (PZT)) [17,18] have been extensively studied. However, the severe size effect leads to poor thickness scalability (commonly limited to 40 nm) and thus a high erase/program voltage of 5 V [19]. This brings challenges for device ministration and low-power operation. Moreover, lead-containing materials should be treated with caution in flexible electronics because of their ability to damage the environment and human health [10]. In addition, organic ferroelectrics, including polyvinylidene fluoride (PVDF)-based polymers and n-nylon, have been used to prepare flexible ferroelectric memory [20,21]. However, their wide applications are hindered by their unsatisfactory thermal stability and high operation voltage. Fortunately, ferroelectricity was discovered in doped HfO_2 films in 2011 [22]. They also exhibit considerable advantages, such as robust scalability, simple chemical composition, and excellent stability, providing a brand-new opportunity for ferroelectric memory. Indeed, the potential of HfO_2-based ferroelectric thin films in flexible electronics has been a research highlight. Li *et al.* [14] prepared a 10 nm Zr-doped HfO_2 film on a flexible PET substrate, confirming its excellent mechanical toughness. In addition, the all-inorganic, transparent, and highly flexible $Hf_{0.85}Ce_{0.15}O_2$ ferroelectric thin films grown on indium tin oxide/mica by the sol-gel method were realized in our previous work [23]. These findings indicate the great potential of HfO_2-based ferroelectric films for flexible electronics applications. However, to integrate ferroelectric thin films into advanced ferroelectric memories, the operating voltage should be further

† Jun-Hui Wang and Tian-Peng Duan contributed equally to this work.

✉ Corresponding authors.
E-mail: J.-J. Liao, liaojiajia@xidian.edu.cn;
Q. Yang, qyang@xtu.edu.cn;
J. Jiang, jiangjie@xtu.edu.cn

reduced on the premise of high remnant polarization [24,25]. Moreover, the wake-up effect in HfO_2-based ferroelectric thin films, represented by the gradually increased polarization as a function of the number of field cycles in the fresh stage, is still a challenge for stable device design. Therefore, it is urgent to develop flexible, wake-up free, and stable ferroelectric thin films with ultra-low operating voltage and high remnant polarization.

In this work, $Hf_{0.5}Zr_{0.5}O_2$ (HZO) ferroelectric films are scaled down via the atomic layer deposition (ALD) method with flexible mica as the substrate. We realized an ultra-low operation voltage of 1.3 V in the HZO thin film, which retains robust ferroelectricity with a remnant polarization ($2P_r$) of 38 μC/cm². Moreover, a robust $2P_r$ of 60 μC/cm² was obtained with an operating voltage of 3 V. The film barely exhibited a wake-up effect because of the suppressed oxygen vacancies at the ferroelectric/metal interfaces. Moreover, the polarization switching mechanism under bending was carefully investigated, indicating the reduced activation field derived from the effects of in-plane stress. The reliability of ultrathin ferroelectric thin films in different service environments was also comprehensively investigated.

2 Experimental

2.1 Fabrication

Fabrication of flexible ferroelectric hafnium-based oxide films: The W bottom electrode was sputtered on a mica substrate [$KMg_3(AlSi_3O_{10})F_2$] (Hefei Kejing Material Technology Co., Ltd., China). Subsequently, the W film as the bottom electrode was sputtered on the mica substrate by the magnetron sputtering technique. Then, HZO films with thicknesses of 6.8, 11.8, and 21.8 nm were grown by ALD. Tetrakis(dimethylamido)hafnium (TDMAH), tetrakis(dimethylamino)zirconium (TDMAZ), and deionized water were used as Hf-, Zr-precursors, and oxygen sources, respectively. In addition, HZO films were grown at 270 °C by adopting Hf-to-Zr ALD cycle ratio of 5:5. After that, W was sputtered as the top electrode via a shadow mask. Finally, all the samples were annealed in N_2 atmosphere at 550 °C for 30 s using a rapid thermal processing system.

2.2 Characterization

Microstructural characterization: To obtain diffraction information, surface morphology, surface phase, and piezoelectric coefficients of ultrathin HZO films, the W top electrode was removed by a solution etching process after post-metallization annealing. The structural properties of HZO thin films were characterized by a grazing incidence X-ray diffractometer (GIXRD; Rigaku Smartlab 9 kW, Japan). The surface morphology, local domain switching characteristics, and piezoelectric response were tested using a piezoelectric force microscope (PFM; Bruker Dimension Icon, Germany). The microstructure of HZO thin films was characterized via a high-resolution transmission electron microscope (HRTEM; FEI TALOS F200X, USA). An energy dispersive X-ray spectroscope (EDX; FEI TALOS F200X, USA) was ultilized to verify the element distributions of the cross-sectional W/HZO/W/mica structure.

Electrical property characterizations: The ferroelectric properties, polarization flipping, endurance, and retention performance of the flexible HZO thin films were determined via a TF 3000 analyzer (aixACCT, Germany) equipped with a heating module. Capacitance versus voltage (C–V), capacitance versus frequency (C–F), and current density versus voltage (J–V) characteristics were evaluated using a semiconductor device parameter analyzer (4200A-SCS, Keithley, USA).

3 Results and discussion

Figure 1(a) shows a photo of the HZO/3 nm W/mica structure and a schematic diagram of the flexible ferroelectric capacitors. The polarization (P)–voltage (V) loops of W/HZO/W/mica with different bottom electrode thicknesses and the corresponding optical transmittance spectra are shown in Fig. S1 in the Electronic Supplementary Material (ESM). When the thickness of the W bottom electrode decreases to 3 nm, the transparency of the HZO/W/mica structure could reach 65%. The 6.8-, 11.8-, and 21.8-nm-thick HZO ferroelectric thin films grown on W/mica were measured by GIXRD with a grazing incidence angle of 0.5°, as shown in Fig. 1(b). To obtain the diffraction information of ultra-thin HZO films, the W top electrode was removed by a solution etching process after post-metallization annealing [15]. The diffraction peak at 27.5° corresponds to substrate $(003)_{mica}$ [26]. The diffraction peaks at 30.5°, 35.5°, and 50° represent the presence of $(111)_o/(101)_t$, $(002)_o/(110)_t$, and $(202)_o/(200)_t$ of HZO, respectively. After the thickness of the HZO film reaches 21.8 nm, diffraction peaks at 28.6° and 31.6° representing the existences of $(\bar{1}11)_m$ and $(111)_m$ appear obviously. Although the diffraction peak at 30.5° might correspond to the orthorhombic (o) and/or tetragonal (t) phases, researchers have demonstrated that this peak is evidence of ferroelectricity in HfO_2-based films [27,28]. The surface morphology of the HZO/W/mica structure with an area of 5 μm × 5 μm exhibits a root-mean-square roughness (R_q) of 425 pm, confirming the flat surface of the HZO film, as presented in Fig. S2 in the ESM. Figure 1(c) shows the local PFM amplitude and phase hysteresis loops of the HZO ferroelectric thin film. The PFM phase curve shows a phase difference of approximately 180°, indicating the ferroelectric switching behavior in HZO. The PFM butterfly curve shows that the film has a good positive piezoelectric coefficient. In addition, we also observed negative piezoelectric effects in other regions of the same sample, as displayed in Fig. S3 in the ESM, which may be due to the coexistence of opposite switching pathways of HfO_2 [29], so that the films have both positive and negative piezoelectric effects. We selected a 3 μm × 3 μm region on the HZO film and applied direct current (DC) voltage with the same magnitude and opposite direction to the left and right sides of this region for "writing" and "erasing" operations. We showed the results in Fig. 1(d). An obvious contrast with a phase difference of 180° and very sharp boundary is found, suggesting that the ferroelectric domains can be completely switched. Our previous work [23,30] reported stable local PFM amplitude and phase hysteresis loops and an out-of-plane PFM piezoresponse phase under bending conditions, which provides a basis for subsequent research on domain flipping dynamics under bending conditions. HRTEM was utilized to further study the microstructure of HZO thin films. Figure 1(e) shows a cross-sectional HRTEM image of the W/HZO/W capacitor on the mica substrate, confirming that the thickness of the HZO film was ~6.8 nm. The fast Fourier transform (FFT) diffractogram pattern of the selected region in the HZO films is displayed in the right panel. This indicates the formation of a ferroelectric phase corresponding to the $[\bar{3}41]$ zone axis of orthorhombic HfO_2. The d-spacings of (212) and (321) crystallographic planes are 1.81 and 1.383 Å, respectively, which is consistent with the theoretical values of the orthorhombic phase HfO_2 ($Pca2_1$) [31,32]. Figure 1(f) shows the EDX elemental mapping of the W/HZO/W/mica structure. The distributions of Hf, Zr, O, W, and Mg elements were characterized by line scanning. The interfaces between each film are clear without mutual diffusion. Figure S4 in the ESM shows an enlarged upper interface of the HRTEM image in Fig. 1(e). There is no obvious WO_x layer at the interface, which suppresses the oxygen vacancies at the W/HZO interface.

Figure 2 shows the performance of HZO ferroelectric thin films on flexible mica substrates with different thicknesses. Figure 2(a) shows the *P*–*V* loops of HZO thin films with varied thickness at

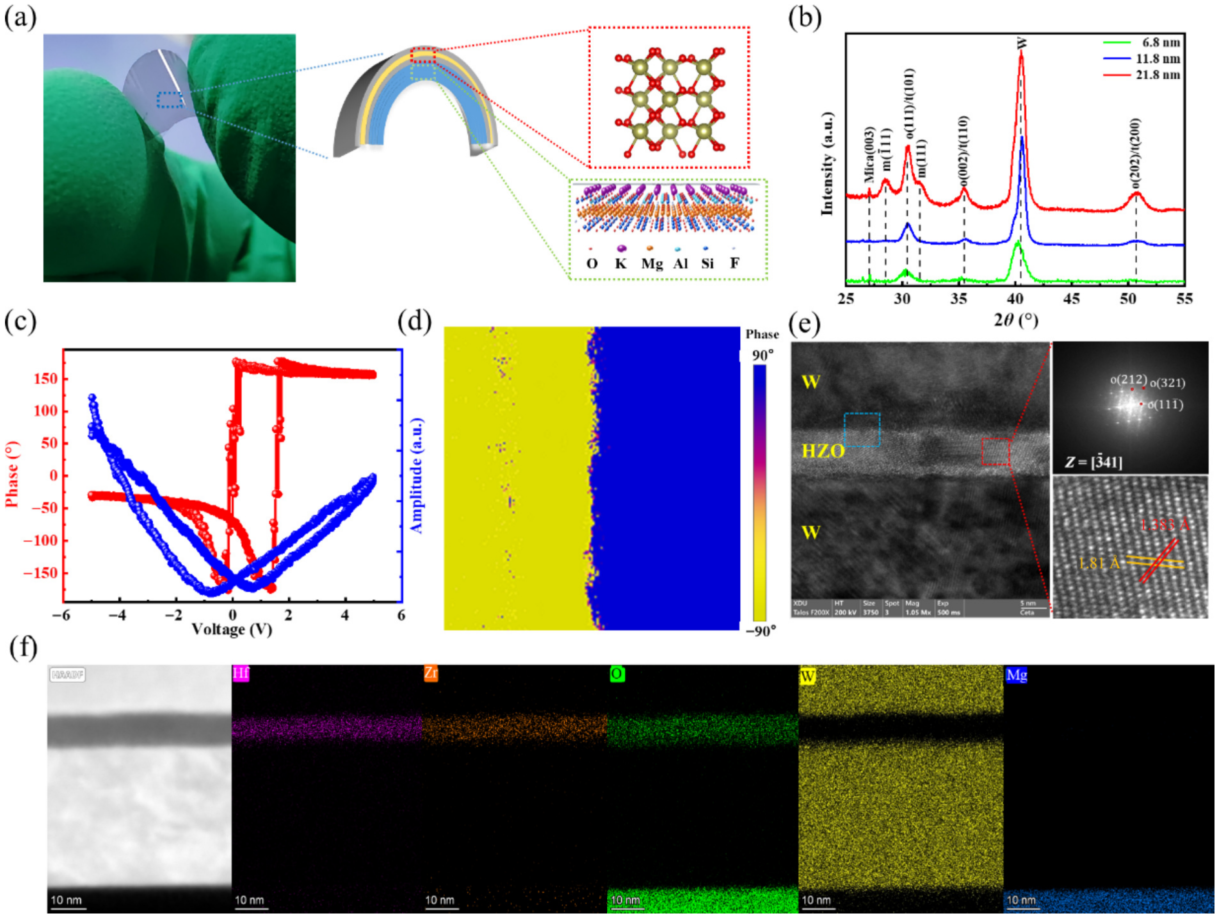

Fig. 1 Photograph and microscopic characterization of HZO ferroelectric capacitors on flexible mica: (a) photograph of HZO/3 nm W/mica structure and schematic diagram of W/HZO/W/mica structure; (b) GIXRD patterns of different thicknesses; (c) local PFM amplitude and phase hysteresis loops, and (d) out-of-plane PFM piezoresponse phase image of HZO/W/mica; (e) HRTEM images of cross-section, and (f) cross-sectional high-angle annular dark-field (HAADF) image and corresponding EDX mapping of W/HZO/W/mica thin films.

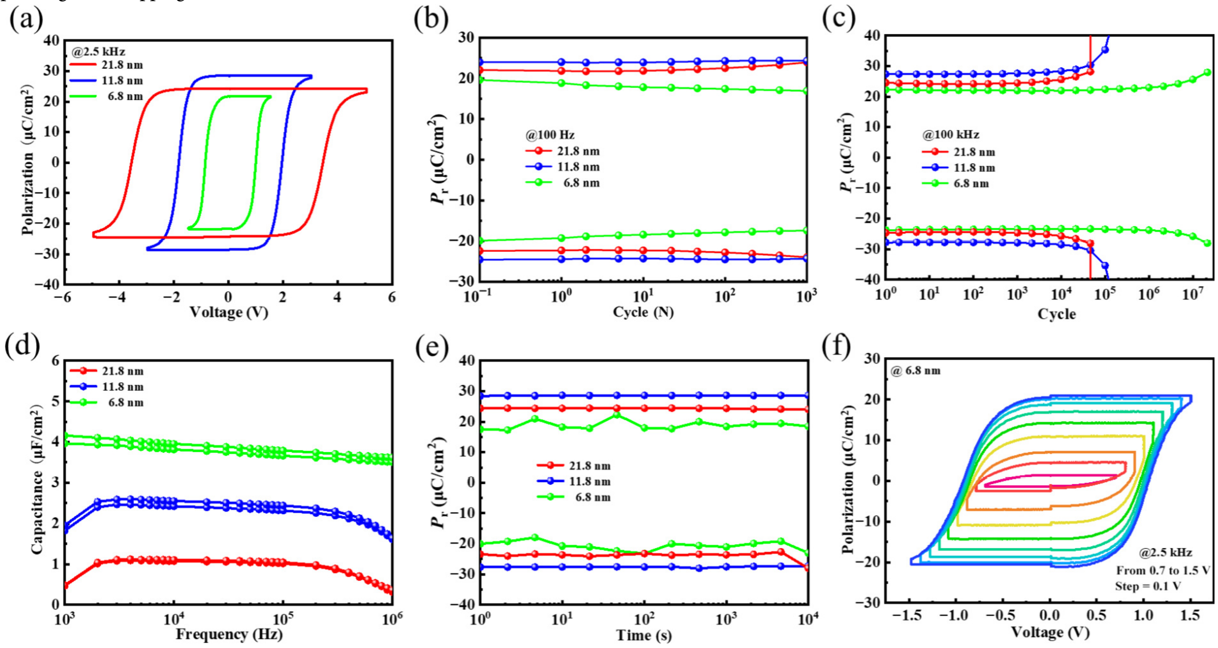

Fig. 2 Performances of ferroelectric capacitors on mica substrates with different HZO thicknesses: (a) *P*–*V* loops obtained by PUND measurement, (b) polarization evolutions during initial field cycling, (c) endurance characteristics, (d) *C*–*F* curves, and (e) retention performance. (f) *P*–*V* loops obtained by PUND measurements of 6.8 nm HZO ferroelectric thin films under different voltages.

positive-up-negative-down (PUND) measurements (for *P*–*E* loops, see Fig. S7(a) in the ESM). The saturation voltage is scaled from 5 V down to 1.5 V as the film thickness is reduced from 21.8 to 6.8 nm. The remnant polarization is enhanced when the thickness of HZO films decreases from 21.8 to 11.8 nm because of the special reverse size effect of HfO_2-based ferroelectrics [33]. This is consistent with the GIXRD results (Fig. 1(b)) that the m-phase clearly exists in the 21.8-nm-thick film. When the film thickness is reduced to 6.8 nm, the $2P_r$ is reduced because of the damage from leakage shielding [34]. The excellent ferroelectricity, with $2P_r$ values of 38 μC/cm², can still be retained in the 6.8-nm-thick film. The polarization evolution of HZO films as a function of the number of field cycles is shown in Fig. 2(b). Repeated rectangular pulses with a frequency of 100 Hz are applied, which are commonly used to "wake up" HfO_2-based ferroelectrics [35,36]. The main causes of the wake-up effect are the transition from t- to o-phases or the transition from amorphous to o-phases, as well as the redistribution of oxygen defects [37]. With the decrease of thickness, the phase components that can undergo t- to o-phases transition and the diffusion of oxygen defects are suppressed. Therefore, the wake-up effect is weakened when the film thickness decreases. The *P*–*V* loops obtained by PUND measurement and *C*–*V* curves of HZO films with different thicknesses before and after the repeated field cycles are displayed in Fig. S5 in the ESM. Moreover, Fig. S6 in the ESM shows the *P*–*V* loops and *I*–*V* curves of HZO films with different thicknesses before and after repeated field cycles. This is mainly due to the high proportion of o-phase after annealing, which suppresses the phase transition. The *C*–*V* curves and dielectric loss curves of HZO with different thicknesses at a test frequency of 100 kHz are shown in Figs. S7(b) and S7(c) in the ESM. Clearly, they all exhibit representative butterfly curves, demonstrating good ferroelectric switching behavior. The *C*–*F* curves with frequencies varying from 1 kHz to 1 MHz are depicted in Fig. 2(d), suggesting better frequency dispersion performance in the 6.8 nm HZO film, which is due to the decrease in defects in thinner films [38]. In addition, the 6.8-nm-thick HZO film exhibits better endurance (i.e., over 2 orders of magnitude greater than that of its counterparts), as shown in Fig. 2(e). The breakdown-type fatigue failure is due mainly to the formation of defect paths. The thicker the film is, the longer the distance for electrons to accelerate; thus, more energy is obtained from the electrons, causing more severe damage to the film [38]. Retention performance of HZO films with different thicknesses after ±1.5, ±3 V, and ±5 V programming/erasing, as illustrated in Fig. 2(e). The P_r value remains essentially unchanged, indicating that the film can still maintain good non-volatile performance after 10^4 s. Figure 2(f) shows the *P*–*V* hysteresis loops of a 6.8 nm HZO film under different voltages obtained by PUND measurement. Figure S7(e) in the ESM shows the statistical graphs of $\pm P_r$ and $\pm V_c$ in Fig. 2(f). We also measured *P*–*E* curves with different pulse heights, as shown in Fig. S7(d) in the ESM. When the voltage reaches 1.3 V, the remnant polarizations of the thin film reach saturation, demonstrating the ultra-low operation voltage. Figure S7(f) in the ESM shows the retention performance of 6.8 nm HZO ferroelectric thin films after ±1.3 V programming/erasing, and the result exactly coincides with that in the case of ±1.5 V. This further demonstrates an ultra-low saturation voltage of 1.3 V.

Figure 3(a) shows test photographs and schematic diagrams with a bending radius of ±2.5 mm under saturated voltage conditions of 1.5 V. The prepared flexible HZO film was fixed on a mold with a bending radius of ±2.5 mm by double-sided adhesives, and the film remained intact. Figure 3(b) shows the *P*–*V* loops of the 6.8 nm HZO thin films with various bending radii during the PUND measurements (for *P*–*E* loops, see Fig. S8(a) in the ESM). When the bending radius is ±12.5 and ±7.5 mm, the saturation remnant polarization ($2P_r$), positive coercive voltage (V^+), and negative coercive voltage (V^-) are approximately 38 μC/cm², +0.95 V, and −0.88 V, respectively. As the bending radius decreases to ±2.5 mm, the coercive voltage is slightly increased, and the $2P_r$ value is slightly decreased. The endurance characteristics under different bending radii are illustrated in Fig. 3(c). Bending radii of ± 12.5 and ± 7.5 mm basically maintain the same fatigue performance as the flat state,

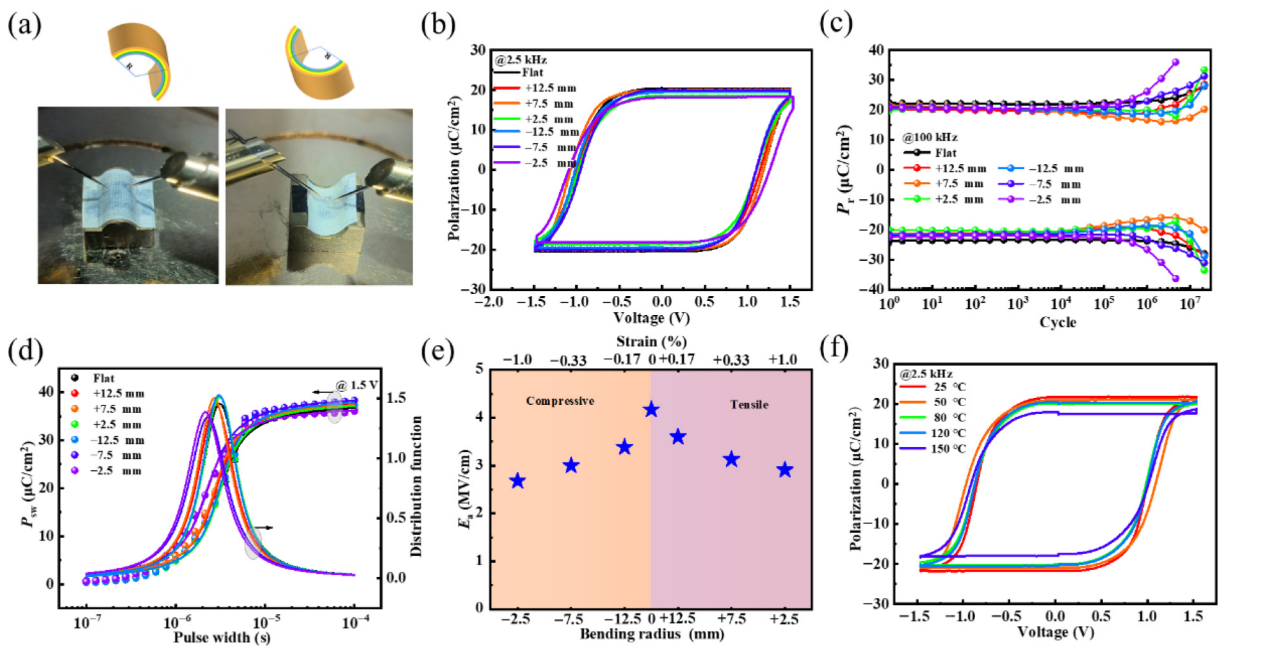

Fig. 3 Performance tests of flexible 6.8 nm HZO ferroelectric thin films under different bending radii: (a) test photos and schematic diagrams with a bending radius of ±2.5 mm; (b) *P*–*V* loops obtained by PUND measurement; (c) endurance characteristics; (d) switched polarization ($\triangle P_{sw}$) as a function of pulse width and Lorentz distribution function. The dots and solid lines represent the experimental data and fitting results according to the nucleation-limited switching (NLS) model. (e) Extracted activation energy under stress. (f) *P*–*V* loops for PUND measurements at different temperatures.

reaching 10^6 cycles. When the bending radius is reduced to ±2.5 mm, the fatigue property decays earlier, indicating a possible slight interface defect [39]. In addition to studying the macroscopic polarization behavior under bending conditions, it is necessary to further explore the domain flipping dynamics. The test principle is shown in Fig. S10 in the ESM. A series of pulses with widths of 100 ns–100 μs were applied to a bent 6.8 nm HZO ferroelectric film with a pulse amplitude of 1.5 V. The pulse width-dependent switched polarization ($\triangle P_{sw}$) is illustrated in the left axis of Fig. 3(d). The right axis of Fig. 3(d) shows the Lorentz distribution of the switching times extracted from the left axis of Fig. 3(d) with a pulse amplitude of 1.5 V. As the bending radius decreases, the switching speed increases slightly, and the switching time distribution widens slightly. This is due to the slight increase in internal defects caused by bending, resulting in a slight decrease in spatial uniformity [40]. In general, the switching speed and switching time distribution remain stable under different bending radii. Moreover, Fig. S11 in the ESM shows the switched polarization $\triangle P_{sw}$ as a function of the pulse width and Lorentz distribution function under Si and mica substrates. By comparison, the extracted ferroelectric domain flipping speeds are 1.69 μs for the mica substrate and 3.5 μs for the Si hard substrate, and the faster domain switching speed in the former might be due to the differences in the W/Si and W/mica interfaces. The former inevitably forms a SiO_2 interfacial layer, such as a voltage divider and a defect-enriched region. This may reduce the domain switching speed. The latter is the van der Waals interface, which is defect free [41]. Therefore, the HZO ferroelectric capacitor grown on mica substrates has a faster domain switching speed. Figure S12 in the ESM shows the polarization switching dynamics for the 6.8-nm-thick HZO film with different top electrode areas. The switching speed increases with the decrease of capacitor area. Through the linear fitting extension line [42], we can expect an ultra-fast switching speed of ~1.2 ns when the capacitor scales down to 1 μm^2. Figure 3(e) shows changes in the activation energy under different strain conditions. Figures S13–S15 in the ESM show fitting diagrams of activation energies with strains of −1%, −0.33%, −0.17%, 0, 0.17%, 0.33%, and 1%, respectively. We discover that the activation energy decreases with increasing strain, which will be discussed later. Furthermore, the temperature dependency of the ferroelectricity of the flexible ferroelectric capacitor was investigated. Figure S8(b) in the ESM shows the *P*–*E* loops of HZO thin films at varied temperatures. According to the *P*–*V* loops obtained by PUND measurement in Fig. 3(f), we confirm the constant remnant polarization when the service temperature is below 120 °C. When the temperature reaches 150 °C, its $2P_r$ slightly decays to 37 $\mu C/cm^2$. It is believed that this phenomenon is related to the change in pyroelectric properties at high temperatures [43,44]. Figure S9 in the ESM shows the *P*–*V* loops for the 11.8-nm HZO ferroelectric thin films under different bending radii and different temperatures. When the bending radius reaches ±2.5 mm and the working temperature reaches 150 °C, excellent ferroelectricity and stability are maintained. Moreover, the *C*–*V* curves are shown in Fig. S8(c) in the ESM, and there is a slight increase in the relative dielectric constant, which is due to an increase in the dipole moment of polar molecules.

Figure 4 systematically compares the operating voltage, service temperature, and $2P_r$ of the flexible HZO ferroelectric films [10–12,14–16,30,45–47]. Obviously, our 6.8 nm flexible HZO film has an ultralow operating voltage of 1.3 V, and the $2P_r$ of the 11.8 nm HZO film reaches 60 $\mu C/cm^2$ at a low operating voltage of 3 V.

To understand the origin of bending-induced variation in the activation electric field, the strain effects on the polarization reversal of [111]-oriented $Pca2_1$-phase HfO_2 were then studied via first principles calculations based on the density functional theory (DFT) approach. Since there is no obvious asymmetry in the ferroelectricity of the bent film, we neglect the bending-induced-strain gradient effect in the calculation.

The DFT calculations were carried out within the Vienna *ab initio* simulation package (VASP) code via the projector-augmented-wave (PAW) method [48]. The Perdew–Burke–Ernzerhof (PBE) generalized gradient approximation (GGA) was used for exchange and correlation functions [49]. The plane wave cutoff energy was set to 450 eV. The first Brillouin zones were sampled by using 5 × 5 × 5 and 7 × 7 × 7 Monkhorst–Pack grids for the [111]-oriented hexagonal cell (with 36 atoms) and conventional orthorhombic unit cell (with 12 atoms) of $Pca2_1$-phase HfO_2, as shown in Fig. 5(a), respectively. The calculated lattice constants for the strain-free [111]-oriented hexagonal HfO_2 cell are 7.28, 7.14, and 8.86 Å, and those of the orthorhombic unit cell are 5.25, 5.04, and 5.07 Å, respectively, which is consistent with previous studies [50]. As shown in Fig. 5(b), the polarization reversal along the C:N pathway with O atoms not through the Hf atomic planes, which has the lowest energy barrier for uniform switching [50], was simulated in the hexagonal cell based on the climbing image nudged elastic band (CI-NEB) approach. The polarization switching energy barrier was calculated to be 0.365 eV per 12 atoms [51], which is in good agreement with that (0.373 eV) obtained in the orthorhombic cell in our previous study [50].

Then, in-plane (IP) biaxial strains were applied to the hexagonal cell by fixing the IP lattice constants and relaxing the out-of-plane (OOP) lattice and all the atoms. Subsequently, the polarization reversal in the strained cells was simulated. Interestingly, it is found that the polarization switching energy barrier decreases when both IP tensile and compressive strains are applied (Fig. 5(c)). This result is in good accordance with our experimental results that the activation electric fields are reduced by both positive and negative curvature bending. Since the same decrease in the energy barrier under tensile and compressive strains seems counterintuitive compared with the generally accepted strain effects, we further examined the variation in the atomic structures in both hexagonal and orthorhombic cells. As shown in Fig. 5(d), the OOP lattice constant (c_0) of the hexagonal cell varies conversely with the IP lattice constants (a_0 and b_0),

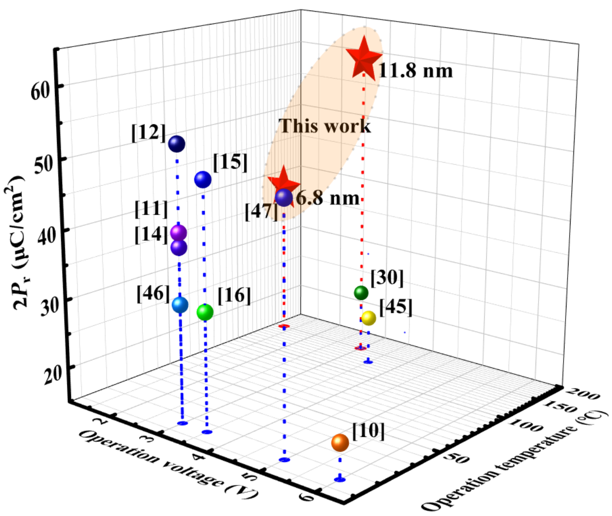

Fig. 4 Benchmarks of $2P_r$, operation voltage, and service temperature for HZO ferroelectric films.

which exhibits a typical positive Poisson's ratio. Then, we plot the variation in the lattice constants (*a*, *b*, and *c*) and angles (α, β, and γ) between the axes of the orthorhombic cell caused by the IP strain in Fig. 5(e). The applied IP strain results in a linear increase in the lattice angle and a slight increase in all three angles. To determine the relationship between the lattice angle and polarization switching energy barrier, we further simulated the polarization reversal in orthorhombic cells with varying lattice angles. As shown in Fig. 5(f), the energy barrier variation agrees well with that obtained in the IP-strained hexagonal cell, confirming that the energy barrier is indeed reduced by increasing and decreasing the lattice angles, which is essentially caused by the IP strain applied to the [111]-oriented hexagonal cell.

To further investigate the effect of bending cycles on flexible 6.8 nm HZO ferroelectric thin films, we repeated bending for 10, 10^2, and 10^3 cycles with a bending diameter of 7.5 mm. Figure S16(a) in the ESM shows the *P*–*E* loops of HZO thin films after different numbers of bending cycles. To remove the effect of leakage current, Fig. 6(a) shows the *P*–*V* loops of HZO thin films with different numbers of bending cycles during the PUND measurement. The remnant polarization and coercive voltage are basically consistent. Figure 6(b) shows the corresponding *C*–*V* curves at a testing frequency of 100 kHz. Clearly, they all exhibit representative butterfly curves, and their relative dielectric constant also remains constant. Figure S16(b) in the ESM shows the dielectric loss curves at a testing frequency of 100 kHz, and we

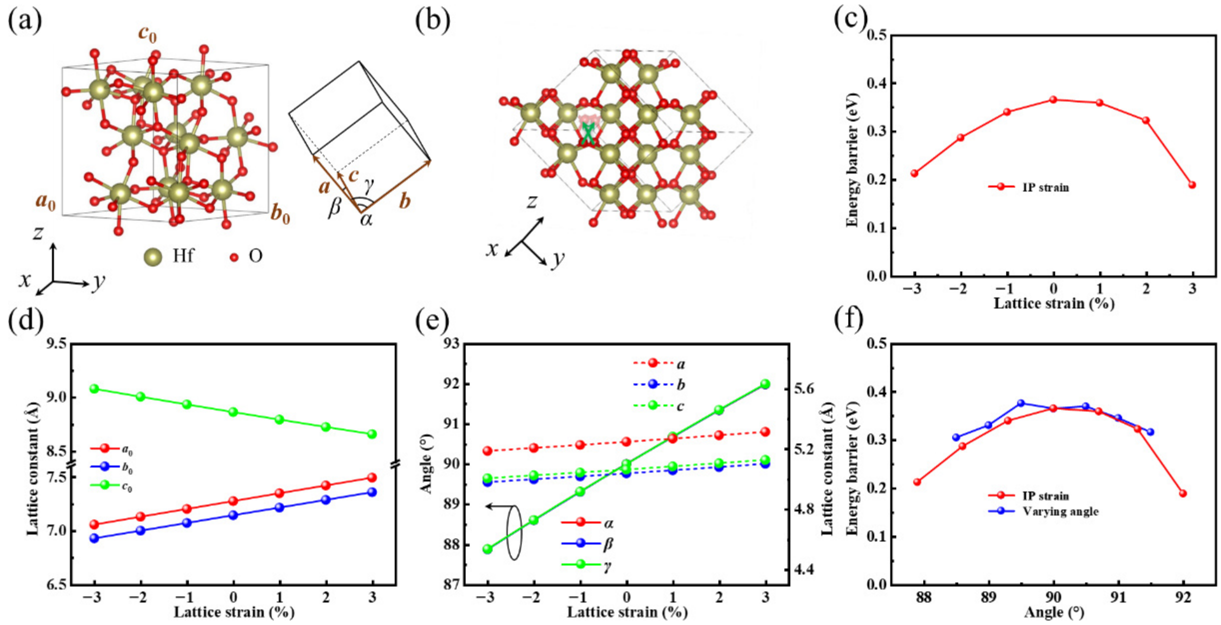

Fig. 5 Crystal structures and polarization switching energy profiles of [111]-oriented orthorhombic HfO_2 under in-plane (IP) strain, as determined via DFT calculations. (a) Crystal structure of [111]-oriented HfO_2. The right panel shows lattice of orthorhombic cell. (b) Polarization switching mode considered in simulation. (c) Polarization switching energy barrier per 12 atoms under applied IP strain. Strain-induced lattice variation in (d) hexagonal and (e) orthorhombic cells. (f) Polarization switching energy barrier varying with lattice angle (blue line). Data in (c) are replotted with red lines for comparison.

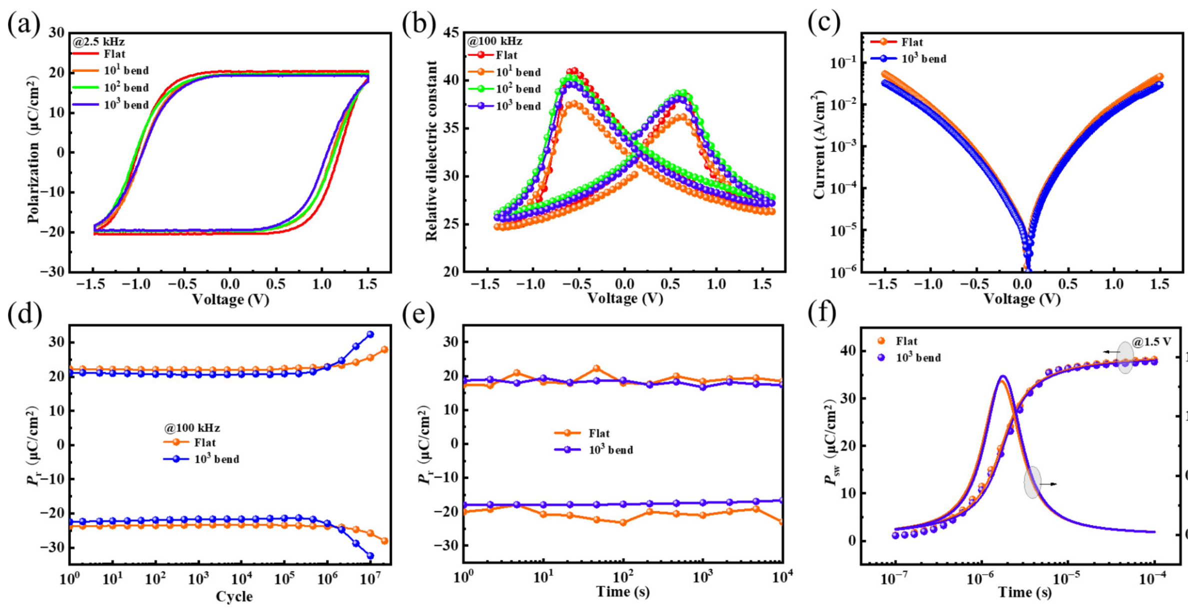

Fig. 6 Performance testing of flexible 6.8 nm HZO thin films after certain bending cycles with a bending diameter of 7.5 mm: (a) *P*–*V* loops obtained by PUND measurement; (b) *C*–*V* curves; (c) *J*–*V* curves; (d) endurance characteristics; (e) retention performance; and (f) switched polarization $\triangle P_{sw}$ as a function of pulse width. The dots and solid lines represent experimental data and fitting results according to NSL model.

find that the dielectric loss basically remains unchanged with increasing number of bending cycles. The non-switching leakage current density is almost independent of the number of bending cycles (Fig. 6 (c)). The endurance performance is shown in Fig. 6(d). After 10^3 cycles of bending, the polarization of the 6.8 nm HZO film changes very little and remains stable at 2×10^7 cycles, as determined by the fatigue resistance test. Retention performance of the 6.8 nm HZO thin films after programming/erasing at ±1.5 V, as shown in Fig. 6(e). After 10^3 cycles of bending, the $2P_r$ value remains basically unchanged, indicating that the film can still maintain good non-volatile performance after 10^4 s. Therefore, the flexible 6.8 nm HZO ferroelectric thin films have good repeatable bending properties. Figure 6(f) shows a series of pulses with widths of 100 ns–100 μs applied to a flexible 6.8 nm HZO ferroelectric film at a voltage of 1.5 V. The dots represent the measured data, and the solid lines are fitted results using the NLS model. Through comparison, it is found that the flipping speed does not change significantly after bending 10^3 times. This further indicates that the thin film has good stability.

Table 1 compares the differences in the basic parameters of flexible ferroelectric thin films between this work and previous works. The organic polymer substrate does not have high temperature resistance, and the thickness of traditional ferroelectric films prepared on mica substrates is too thick for micro integration; the operating voltage of the HZO film prepared on mica substrates is greater than 3 V, which is not conducive to the preparation of portable devices. However, the 6.8 nm HZO ferroelectric film prepared on mica substrates in this study has high ferroelectric properties, ultra-low operating voltage of 1.3 V, high operating temperature of 150 °C, and excellent bending resistance, which is very suitable for the preparation of portable devices.

Table 1 Comparison of several flexible ferroelectric memory elements

Ferroelectric material	Substrate	Deposition technique	Thickness (nm)	Polarization (μC/cm²)	Operation voltage (V)	Minimum bending radius (mm)	Working temperature (°C)	Ref.
HZO	PI	ALD	30	20	±6.0	5.0	25	[10]
HZO	PI	ALD	10	42	±3.0	2.0	25	[11]
HZO	PI	ALD	10	54	±3.0	5.0	25	[12]
P(VDF-TrFE)	PEN	Spin-coating	120	17	±24.0	7.0	25	[13]
HZO	PET	ALD	10	40	±3.0	3.0	25	[14]
HZO	Mica	ALD	10	50	±3.5	2.0	25	[15]
HZO	Mica	ALD	8	32	±3.5	5.0	25	[16]
PZT	Mica	PLD	180	98	±10.0	4.0	200	[17]
PZT	Mica	PLD	500	80	±5.0	5.0	200	[18]
$Hf_{0.85}Ce_{0.15}O_2$	Mica	Sol–gel	116	32	±37.0	2.5	150	[23]
$Hf_{0.6}Zr_{0.4}O_2$	Mica	ALD	15	24	±3.0	±5.0	150	[30]
HZO	Mica	ALD	18	22	±3.5	7.5	125	[45]
HZO	Mica	ALD	20	32	±3.0	4.0	25	[46]
HZO	Mica	ALD	11.4	50	±5.0	5.0	25	[47]
HZO	Mica	ALD	6.8/11.8	38/60	±1.3/3.0	±2.5	150	This work

4 Conclusions

In summary, we realized flexible, wake-up free, and stable HZO ferroelectric films with ultra-low operation voltage (1.3/3 V) and robust polarization ($2P_r$ of 38/60 μC/cm²). The high service temperature of 150 °C and up to 10^3 cycles of bending are also demonstrated for the flexible thin films. Within a ±2.5 mm bending radius, HZO thin films show stable remnant polarization, robust fatigue resistance, and retention properties. In addition, we carefully investigated the impact of bending on the polarization switching properties and found that the distribution of the polarization switching time remained similar to the change in the bending radius and the activation field was negatively correlated with the compressive and tensile stresses. Finally, we computationally demonstrated that the reduced activation field under bending was due to the lowered energy barrier induced by the in-plane strain applied to the [111]-oriented hexagonal cell. This work provides a solid foundation experimentally and theoretically to adopt the HfO_2-based ferroelectric thin films in various flexible devices, such as electronic displays, flexible ferroelectric memory, and wearable devices.

Acknowledgements

This work was supported by the National Natural Science Foundation of China (Nos. 12372331, 12302429, 11932016, and 12072307); the Outstanding Youth Science Foundation of Hunan Province, China (No. 2021JJ20041); the Department of Education Project of Hunan Province, China (No. 21B0112); the Innovation Capability Support Program of Shaanxi (No. 2022TD-28); and the Guangdong Basic and Applied Basic Research Foundation (No. 2022A1515110116). We also acknowledge the Instrumental Analysis Center of Xidian University for providing test equipment.

Declaration of competing interest

The authors have no competing interests to declare that are relevant to the content of this article.

Electronic Supplementary Material

Supplementary material is available in the online version of this article at https://doi.org/10.26599/JAC.2024.9220981.

References

[1] Zhang F, Hu HL, Hu SM, *et al.* Significant strain-rate dependence of sensing behavior in TiO_2@carbon fibre/PDMS composites for flexible strain sensors. *J Adv Ceram* 2021, **10**: 1350–1359.

[2] Liu YH, Pharr M, Salvatore GA. Lab-on-skin: A review of flexible and stretchable electronics for wearable health monitoring. *ACS Nano* 2017, **11**: 9614–9635.

[3] Jung YH, Chang TH, Zhang HL, *et al.* High-performance green flexible electronics based on biodegradable cellulose nanofibril paper. *Nat Commun* 2015, **6**: 7170.

[4] Hao YX, Xie JW, Xu BQ, *et al.* Tunnel elasticity enhancement effect of 3D submicron ceramics (Al_2O_3, TiO_2, ZrO_2) fiber on polydimethylsiloxane (PDMS). *J Adv Ceram* 2021, **10**: 502–508.

[5] Heo JS, Eom J, Kim YH, *et al.* Recent progress of textile-based wearable electronics: A comprehensive review of materials, devices, and applications. *Small* 2018, **14**: 1703034.

[6] Han ST, Peng HY, Sun QJ, *et al.* An overview of the development of flexible sensors. *Adv Mater* 2017, **29**: 1700375.

[7] Hao PQ, Zheng SZ, Zeng BJ, *et al.* Highly enhanced polarization switching speed in HfO_2-based ferroelectric thin films via a composition gradient strategy. *Adv Funct Mater* 2023, **33**: 2301746.

[8] Bao KY, Liao JJ, Yan F, *et al.* Enhanced endurance and imprint properties in $Hf_{0.5}Zr_{0.5}O_{2-\delta}$ ferroelectric capacitors by tailoring the oxygen vacancy. *ACS Appl Electron Mater* 2023, **5**: 4615–4623.

[9] Takagi S, Toprasertpong K, Tahara K, *et al.* HfZrO-based ferroelectric devices for lower power AI and memory applications. *ECS Transactions* 2021, **104**: 17.

[10] Yu H, Chung CC, Shewmon N, *et al.* Flexible inorganic ferroelectric thin films for nonvolatile memory devices. *Adv Funct Mater* 2017, **27**: 1700461.

[11] Chen YT, Yang Y, Yuan P, *et al.* Flexible $Hf_{0.5}Zr_{0.5}O_2$ ferroelectric thin films on polyimide with improved ferroelectricity and high flexibility. *Nano Res* 2022, **15**: 2913–2918.

[12] Chouprik A, Mikheev V, Margolin I, *et al.* Superflexible and stretchable ferroelectric memory on a biocompatible platform. *Adv Elect Mater* 2024, **10**: 2300449.

[13] Lee GH, Yu YJ, Lee CG, *et al.* Electron tunneling through atomically flat and ultrathin hexagonal boron nitride. *Appl Phys Lett* 2011, **99**: 243114.

[14] Liu BW, Zhang YR, Zhang LJ, *et al.* Excellent HZO ferroelectric thin films on flexible PET substrate. *J Alloys Compd* 2022, **919**: 165872.

[15] Joh H, Jung M, Hwang J, *et al.* Flexible ferroelectric hafnia-based synaptic transistor by focused-microwave annealing. *ACS Appl Mater Inter* 2022, **14**: 1326–1333.

[16] Zhou X, Sun H, Li J, *et al.* A flexible $Hf_{0.5}Zr_{0.5}O_2$ thin film with highly robust ferroelectricity. *J Materiomics* 2024, **10**: 210–217.

[17] Jiang J, Bitla Y, Huang CW, *et al.* Flexible ferroelectric element based on van der Waals heteroepitaxy. *Sci Adv* 2017, **3**: e1700121.

[18] Tsai MF, Jiang J, Shao PW, *et al.* Oxide heteroepitaxy-based flexible ferroelectric transistor. *ACS Appl Mater Inter* 2019, **11**: 25882–25890.

[19] Ghoneim MT, Zidan MA, Alnassar MY, *et al.* Thin PZT-based ferroelectric capacitors on flexible silicon for nonvolatile memory applications. *Adv Elect Mater* 2015, **1**: 1500045.

[20] Li MY, Wondergem HJ, Spijkman MJ, *et al.* Revisiting the δ-phase of poly(vinylidene fluoride) for solution-processed ferroelectric thin films. *Nat Mater* 2013, **12**: 433–438.

[21] Anwar S, Pinkal D, Zajaczkowski W, *et al.* Solution-processed transparent ferroelectric nylon thin films. *Sci Adv* 2019, **5**: eaav3489.

[22] Böscke TS, Müller J, Bräuhaus D, *et al.* Ferroelectricity in hafnium oxide thin films. *Appl Phys Lett* 2011, **99**: 102903.

[23] Mo ST, Feng KM, Pang JL, *et al.* All-inorganic transparent $Hf_{0.85}Ce_{0.15}O_2$ ferroelectric thin films with high flexibility and stability. *Nano Res* 2023, **16**: 5065–5072.

[24] Okuno J, Kunihiro T, Konishi K, *et al.* High-endurance and low-voltage operation of 1T1C FeRAM arrays for nonvolatile memory application. In: Proceedings of the IEEE International Memory Workshop, Dresden, Germany, 2021: 1–3.

[25] Kawashima S, Endo T, Yamamoto A, *et al.* Bitline GND sensing technique for low-voltage operation FeRAM. *IEEE J Solid State Circuits* 2002, **37**: 592–598.

[26] Ouyang K, Duan TP, Huang WQ, *et al.* Large-scale, high-transparency, ultra-thin ITO membranes with robust conductivity and flexibility. *Acta Mater* 2023, **260**: 119334.

[27] Zeng B J, Xie S C, Zhang S R, *et al.* Polarization fatigue mechanism of laminated hafnium zirconium oxide ferroelectric thin films. *Acta Mater* 2024, **272**: 119920.

[28] Liu C, Yang QJ, Zeng BJ, *et al.* Orientation independent growth of uniform ferroelectric $Hf_{0.5}Zr_{0.5}O_2$ thin films on silicon for high-density 3D memory applications. *Adv Funct Mater* 2022, **32**: 2209604.

[29] Qi YB, Reyes-Lillo SE, Rabe KM. "Double-path" ferroelectrics and the sign of the piezoelectric response. *arXiv preprint* 2022, arXiv: 2204.06999.

[30] Liu WY, Liao JJ, Jiang J, *et al.* Highly stable performance of flexible $Hf_{0.6}Zr_{0.4}O_2$ ferroelectric thin films under multi-service conditions. *J Mater Chem C* 2020, **8**: 3878–3886.

[31] Wei YF, Nukala P, Salverda M, *et al.* A rhombohedral ferroelectric phase in epitaxially strained $Hf_{0.5}Zr_{0.5}O_2$ thin films. *Nat Mater* 2018, **17**: 1095–1100.

[32] Zeng BJ, Liu C, Dai SW, *et al.* Electric field gradient-controlled domain switching for size effect-resistant multilevel operations in HfO_2-based ferroelectric field-effect transistor. *Adv Funct Mater* 2021, **31**: 2011077.

[33] Cheema SS, Kwon D, Shanker N, *et al.* Enhanced ferroelectricity in ultrathin films grown directly on silicon. *Nature* 2020, **580**: 478–482.

[34] Matveyev Y, Negrov D, Chernikova A, *et al.* Effect of polarization reversal in ferroelectric TiN/$Hf_{0.5}Zr_{0.5}O_2$/TiN devices on electronic conditions at interfaces studied in operando by hard X-ray photoemission spectroscopy. *ACS Appl Mater Inter* 2017, **9**: 43370–43376.

[35] Zhang S, Zhang Q, Meng F, *et al.* Domain wall evolution in $Hf_{0.5}Zr_{0.5}O_2$ ferroelectrics under field-cycling behavior. *Research* 2023, **6**: 0093.

[36] Zhou PG, Zeng BJ, Yang WZ, *et al.* Intrinsic 90° charged domain wall and its effects on ferroelectric properties. *Acta Mater* 2022, **232**: 117920.

[37] Liao JJ, Dai SW, Peng RC, *et al.* HfO_2-based ferroelectric thin film and memory device applications in the post-Moore era: A review. *Fundam Res* 2023, **3**: 332–345.

[38] Park MH, Kim HJ, Kim YJ, *et al.* Study on the internal field and conduction mechanism of atomic layer deposited ferroelectric $Hf_{0.5}Zr_{0.5}O_2$ thin films. *J Mater Chem C* 2015, **3**: 6291–6300.

[39] Hsain HA, Lee Y, Lancaster S, *et al.* Reduced fatigue and leakage of ferroelectric TiN/$Hf_{0.5}Zr_{0.5}O_2$/TiN capacitors by thin alumina interlayers at the top or bottom interface. *Nanotechnology* 2023, **34**: 125703.

[40] Lee DH, Yu GT, Park JY, *et al.* Effect of residual impurities on polarization switching kinetics in atomic-layer-deposited ferroelectric $Hf_{0.5}Zr_{0.5}O_2$ thin films. *Acta Mater* 2022, **222**: 117405.

[41] Wang QS, Safdar M, Xu K, *et al.* Van der waals epitaxy and photoresponse of hexagonal tellurium nanoplates on flexible mica sheets. *ACS Nano* 2014, **8**: 7497–7505.

[42] Jiang Y, Parsonnet E, Qualls A, *et al.* Enabling ultra-low-voltage switching in $BaTiO_3$. *Nat Mater* 2022, **21**: 779–785.

[43] Lomenzo PD, Jachalke S, Stoecker H, *et al.* Universal Curie constant and pyroelectricity in doped ferroelectric HfO_2 thin films. *Nano Energy* 2020, **74**: 104733.

[44] Jachalke S, Schenk T, Park MH, *et al.* Pyroelectricity of silicon-doped hafnium oxide thin films. *Appl Phys Lett* 2018, **112**: 142901.

[45] Xiao WW, Liu C, Peng Y, *et al.* Thermally stable and radiation hard ferroelectric $Hf_{0.5}Zr_{0.5}O_2$ thin films on muscovite mica for flexible nonvolatile memory applications. *ACS Appl Electron Mater* 2019, **1**: 919–927.

[46] Liu HF, Lu TQ, Li YX, *et al.* Flexible quasi-van der Waals ferroelectric hafnium-based oxide for integrated high-performance nonvolatile memory. *Adv Sci* 2020, **7**: 2001266.

[47] Li QX, Wang SW, Li ZH, *et al.* High-performance ferroelectric field-effect transistors with ultra-thin indium tin oxide channels for flexible and transparent electronics. *Nat Commun* 2024, **15**: 2686.

[48] Kresse G, Joubert D. From ultrasoft pseudopotentials to the projector augmented-wave method. *Phys Rev B* 1999, **59**: 1758–1775.

[49] Perdew JP, Burke K, Ernzerhof M. Generalized gradient approximation made simple. *Phys Rev Lett* 1996, **77**: 3865–3868.

[50] Wu Y, Zhang YK, Jiang J, *et al.* Unconventional polarization-switching mechanism in (Hf,Zr)O_2 ferroelectrics and its implications. *Phys Rev Lett* 2023, **131**: 226802.

[51] Henkelman G, Uberuaga BP, Jónsson H. A climbing image nudged elastic band method for finding saddle points and minimum energy paths. *J Chem Phys* 2000, **113**: 9901–9904.